UNIVERSITY OF AMSTERDAM

UvA-DARE (Digital Academic Repository)

No Measurable Changes in Radio and X-Ray Emission Surrounding Glitches in the Young Pulsar PSR J2229+6114

Xia, Wenke; Main, Robert; Ng, Mason; Kaspi, Victoria M.; Hessels, Jason W.T.; Cassity, Alyssa; Denney, Abigail K.; Fonseca, Emmanuel; Good, Deborah C.; Kumar, Ajay; Künkel, Lars; Meyers, Bradley W.; Pearlman, Aaron B.; Stairs, Ingrid

DOI
10.3847/1538-4357/ae9758

Publication date
2026

Document Version
Final published version

Published in
Astrophysical Journal

License
CC BY

Link to publication

Citation for published version (APA):
Xia, W., Main, R., Ng, M., Kaspi, V. M., Hessels, J. W. T., Cassity, A., Denney, A. K., Fonseca, E., Good, D. C., Kumar, A., Künkel, L., Meyers, B. W., Pearlman, A. B., & Stairs, I. (2026). No Measurable Changes in Radio and X-Ray Emission Surrounding Glitches in the Young Pulsar PSR J2229+6114. *Astrophysical Journal*, *1008*(1), Article 100. https://doi.org/10.3847/1538-4357/ae9758

General rights
It is not permitted to download or to forward/distribute the text or part of it without the consent of the author(s) and/or copyright holder(s), other than for strictly personal, individual use, unless the work is under an open content license (like Creative Commons).

Disclaimer/Complaints regulations
If you believe that digital publication of certain material infringes any of your rights or (privacy) interests, please let the Library know, stating your reasons. In case of a legitimate complaint, the Library will make the material inaccessible and/or remove it from the website. Please Ask the Library: https://uba.uva.nl/en/contact, or a letter to: Library of the University of Amsterdam, Secretariat, P.O. Box 19185, 1000 GD Amsterdam, The Netherlands. You will be contacted as soon as possible.

UvA-DARE is a service provided by the library of the University of Amsterdam (https://dare.uva.nl)

Download date:17 Nov 2026

The Astrophysical Journal, 1008:100 (10pp), 2026 September 1 https://doi.org/10.3847/1538-4357/ae9758
© 2026. The Author(s). Published by the American Astronomical Society.
OPEN ACCESS

No Measurable Changes in Radio and X-Ray Emission Surrounding Glitches in the Young Pulsar PSR J2229+6114

Wenke Xia[1,2], Robert Main[1,2], Mason Ng[1,2], Victoria M. Kaspi[1,2], Jason W. T. Hessels[1,2,3,4], Alyssa Cassity[5], Abigail K. Denney[6], Emmanuel Fonseca[7,8], Deborah C. Good[9], Ajay Kumar[10], Lars Künkel[1,2], Bradley W. Meyers[11,12], Aaron B. Pearlman[1,2,13,14,15], and Ingrid Stairs[5]
[1] Department of Physics, McGill University, 3600 rue University, Montréal, QC H3A 2T8, Canada; wenke.xia@mail.mcgill.ca
[2] Trottier Space Institute, McGill University, 3550 rue University, Montréal, QC H3A 2A7, Canada
[3] Anton Pannekoek Institute for Astronomy, University of Amsterdam, Science Park 904, 1098 XH Amsterdam, The Netherlands
[4] ASTRON, Netherlands Institute for Radio Astronomy, Oude Hoogeveensedijk 4, 7991 PD Dwingeloo, The Netherlands
[5] Department of Physics and Astronomy, University of British Columbia, 6224 Agricultural Road, Vancouver, BC V6T 1Z1, Canada
[6] David A. Dunlap Department of Astronomy and Astrophysics, University of Toronto, 50 St. George Street, ON M5S 3H4, Canada
[7] Department of Physics and Astronomy, West Virginia University, P.O. Box 6315, Morgantown, WV 26506, USA
[8] Center for Gravitational Waves and Cosmology, West Virginia University, Chestnut Ridge Research Building, Morgantown, WV 26505, USA
[9] Department of Physics and Astronomy, University of Montana, 32 Campus Drive, Missoula, MT 59812, USA
[10] National Centre for Radio Astrophysics, Post Bag 3, Ganeshkhind, Pune, 411007, India
[11] Australian SKA Regional Centre (AusSRC), Curtin University, Bentley, WA 6102, Australia
[12] International Centre for Radio Astronomy Research (ICRAR), Curtin University, Bentley, WA 6102, Australia
[13] Department of Physics, Massachusetts Institute of Technology, 77 Massachusetts Ave, Cambridge, MA 02139, USA
[14] MIT Kavli Institute for Astrophysics and Space Research, Massachusetts Institute of Technology, 77 Massachusetts Ave, Cambridge, MA 02139, USA
Received 2026 May 13; revised 2026 July 8; accepted 2026 August 6; published 2026 August 27

Abstract

We present our first result from an ongoing pulsar glitch monitoring campaign at the Canadian Hydrogen Intensity Mapping Experiment (CHIME), in which we analyzed the radio and X-ray emission surrounding four glitches in PSR J2229+6114. Using daily CHIME observations, we detected a glitch in PSR J2229+6114 in near-real time and triggered an X-ray follow-up with the Nuclear Spectroscopic Telescope Array (NuSTAR) two days after the glitch. We identified three additional glitch events in archival CHIME/Pulsar observations that coincided with an independent X-ray observing campaign with the Neutron star Interior Composition Explorer (NICER). Our data show there is no measurable change in the source's X-ray and radio emission during the four glitch events, in stark contrast to the postglitch activity in high-magnetic-field, rotation-powered pulsars (RPPs), which have been observed to exhibit magnetar-like X-ray outbursts immediately after large glitches. Those high-magnetic-field (high-B) RPPs are considered transitional objects between ordinary RPPs and magnetars, thereby leading to a unifying neutron star model in which the inferred dipolar surface magnetic field strength serves as a unifying parameter. However, such a model remains challenged, in part, by the lack of constraints near the low-B end of the high-B regime, and our result provides additional evidence that magnetar-like postglitch activity is likely more common among high-B RPPs.

Unified Astronomy Thesaurus concepts: Rotation powered pulsars (1408); Magnetars (992)

1. Introduction

Pulsars and magnetars are typically classified as two distinct types of neutron stars, largely due to their different emission properties and activities. Conventional rotation-powered pulsars (RPPs) are generally radio-loud, exhibiting stable thermal X-ray emission from surface cooling. Magnetars, on the other hand, are not commonly visible in the radio band and are primarily powered by their decaying internal magnetic fields, and they exhibit more frequent outbursts and variations in their X-ray emission. Magnetars also differ in their spin properties. Assuming magnetic dipole braking, magnetars generally show surface dipolar magnetic field strengths (hereafter "B-field") of the order of $B_{\rm dip} \approx 10^{14}$–$10^{15}$ G,[16] much higher than typical RPPs that usually have $B_{\rm dip} \lesssim 10^{14}$ G. Both classes exhibit rotational glitches, but postglitch activity in magnetars is often more dramatic, accompanied by X-ray outbursts or pulse profile variations (see V. M. Kaspi & A. M. Beloborodov 2017 for a review).

Despite the apparent differences in properties of pulsars and magnetars, this dichotomous classification is challenged by the transient magnetar-like X-ray bursting behavior in two high-magnetic-field ($B_{\rm dip} \approx 10^{13}$–$10^{14}$ G; hereafter "high-B") RPPs, PSRs J1846−0258 (F. P. Gavriil et al. 2008; C.-P. Hu et al. 2023) and J1119−6127 (R. F. Archibald et al. 2016), immediately after large spin-up glitch events ($\Delta\nu/\nu > 10^{-6}$). These discoveries argue that high-B RPPs in the potentially magnetar-strength inferred B-field regime (from 10^{13} to 10^{14} G; hereafter "high-B RPP regime") are also transitional objects in the neutron star population that bridge the emission and bursting behaviors of pulsars and magnetars. They suggest a unified neutron star model in which the inferred B-field serves as a unifying parameter in bursting behavior across the phenomenological gap between RPPs and magnetars (V. M. Kaspi 2010; R. Perna & J. A. Pons 2011). In addition to radiative changes at X-ray energies, PSR J1119−6127 also exhibited radio profile variations after a large glitch

[15] NASA Hubble Fellow.
[16] The surface dipolar B-field is given as $B_{\rm dip} = 3.2 \times 10^{19}\,{\rm G} \times \sqrt{P\dot{P}}$, for the pulse period P (in seconds), and the spin-down rate $\dot{P}$ (unitless). Magnetars can exhibit larger, more localized multipole components that may significantly exceed the inferred $B_{\rm dip}$ value.

Original content from this work may be used under the terms of the Creative Commons Attribution 4.0 licence. Any further distribution of this work must maintain attribution to the author(s) and the title of the work, journal citation and DOI.

(P. Weltevrede et al. 2011). Despite similar sudden profile changes being observed in lower B-field RPPs through various mechanisms, those changes are believed to be different phenomena that are unrelated to glitch events (e.g., PSRs J1643−1224 of P. R. Brook et al. 2018 and J1713 +0747 of R. J. Jennings et al. 2024).

While this unifying picture is consistent with existing evidence, a more robust confirmation still requires consideration of the behavior of RPPs near the lower end of the high-B RPP regime (from 10^{12} to 10^{13} G). To fill this gap, we have developed a daily-cadence pulsar monitoring campaign by leveraging the capability of daily all-sky revisits at the Canadian Hydrogen Intensity Mapping Experiment (CHIME) telescope, using its CHAMPSS (C. Andrade et al. 2025) and CHIME/Pulsar (CHIME/Pulsar Collaboration et al. 2021) digital instruments. Such a dedicated high-cadence monitoring campaign is necessary to robustly test the unifying model near the lower end of the high-B RPP regime for two primary reasons. First, magnetar-like X-ray emission and bursts from postglitch RPPs decay on timescales of weeks to months (e.g., two months for PSR J1846−0258; F. P. Gavriil et al. 2008); follow-up observations are required immediately after the glitch (usually within days). On the other hand, the glitch-induced radiative change in RPPs may be faint and therefore not detectable by existing all-sky X-ray monitors.

On 2026 March 9, a glitch in the RPP PSR J2229+6114 was detected by our near-real-time glitch alert system that we built for our monitoring campaign. PSR J2229+6114 is an energetic young "Vela-like" RPP with a spin period of 51.6 ms (J. P. Halpern et al. 2001). It has a spin-inferred surface dipolar B-field of 2.0×10^{12} G (R. N. Manchester et al. 2005), placing it immediately below the high-B RPP regime. We thereby triggered an X-ray follow-up through our target-of-opportunity (ToO) observation with the Nuclear Spectroscopic Telescope Array (NuSTAR) mission approximately two days after the glitch occurred. We also identified three other glitch events in archival observations from the CHIME/Pulsar instrument, which were fortuitously observed in X-rays by a different monitoring campaign with the Neutron star Interior Composition Explorer (NICER) mission.

In this paper, we present an analysis of radio and X-ray emission from PSR J2229+6114 surrounding four glitch events. In Section 2, we describe observations obtained by two instruments at the CHIME telescope (CHAMPSS and CHIME/Pulsar) and two X-ray space missions (NuSTAR and NICER), along with the preprocessing procedures applied to prepare the data for further analysis. We then detail the detection and modeling of the four glitch events in Section 3. We show results from radio and X-ray emission analysis in Sections 4 and 5, respectively, including X-ray flux analyses, pulse profile morphology in both bands, and searches for burst activity. In Section 6, we present our result alongside four previous postglitch X-ray follow-ups of RPPs and discuss the implications of these measurements for the unified neutron star model. We conclude and outline our future prospects in Section 7.

2. Observations and Preprocessing

2.1. CHAMPSS and CHIME/Pulsar Observations

CHIME is a transit telescope operating at a radio frequency of 400–800 MHz (CHIME Collaboration et al. 2022). Our radio observations are recorded by the CHAMPSS and CHIME/Pulsar, two independent digital instruments at the telescope.

CHAMPSS is a pulsar survey instrument that uses the beamformed intensity data stream from CHIME/FRB at a time resolution of 0.983 ms. It stitches together the time series recorded from adjacent CHIME/FRB steady beams along the east–west direction to perform a pulsar periodicity search. Starting with the stitched time series, we can follow up known transiting sources by dedispersing the data incoherently at a known dispersion measure (DM) and folding the resulting data product into an "archive" file (see C. Andrade et al. 2025 for technical details). For PSR J2229+6114, the instrument records data for ∼13.4 minutes during the transit of the source in the CHIME field of view. The folded data archive for the source contains a 3D cube of 1024 frequency channels, 81 time subintegrations, and 32 phase bins in PSRCHIVE format (A. W. Hotan et al. 2004). CHAMPSS recorded data for the source from 2026 January 21 to 2026 April 9 (MJDs 61061 to 61139).

CHIME/Pulsar is a dedicated pulsar observing instrument that forms digital tracking beams from CHIME raw voltage (baseband) data. After beamforming, it coherently dedisperses the beamformed baseband data at a known DM and folds the data into PSRCHIVE archive files with a fixed resolution of 1024 frequency channels (see CHIME/Pulsar Collaboration et al. 2021 for technical details). The instrument records data for PSR J2229+6114 during the source's full transit in the CHIME field of view for ∼30 minutes (i.e., the time that the source drifts across the FWHM of the CHIME beam at 400 MHz). It has then been configured to save "archive" files with 256 rotational phase bins, 59 subintegrations, and four polarization products of XX^*, YY^*, Re(XY^*), Im(XY^*) for the source. CHIME/Pulsar started observing the source on 2020 January 7 (MJD 58855), and we used all the data through 2024 July 22 (MJD 60513).

Folded archives from both digital instruments are further reduced by a pipeline processing to extract times of arrival (TOAs) for subsequent timing analysis. Radio-frequency interference (RFI) in the data is first mitigated using the `clfd` package (V. Morello et al. 2019). Then, the data cube in each archive is summed over polarization (for CHIME/Pulsar data), frequency, and time to produce a 1D pulse profile using the `pam` program in PSRCHIVE. We obtained a standard profile template by fitting von Mises profiles on an observed profile using the `paas` program. We subsequently used the Fourier domain with the Markov Chain Monte Carlo (FDM) shift algorithm embedded in the PSRCHIVE `pat` program to extract TOAs. Each TOA in our timing dataset corresponds to a single observation recorded during the telescope's daily transit.

2.2. NuSTAR Observations

NuSTAR observed PSR J2229+6114 through a triggered ToO observation starting on 2026 March 11 at 21:00:10 UTC (MJD 61110.88; ObsID 81102350002), roughly two days after the detection of the glitch. To compare the postglitch emission with the preglitch levels, we also downloaded the only archival NuSTAR observation available on the HEASARC Browse interface[17] from 2020 September 23 (MJD 59113.99; ObsID 40660001002).

[17] https://heasarc.gsfc.nasa.gov

The standard pipeline tools (`nupipeline` and `nuproducts`) in NuSTARDAS v2.1.5 were used for data reduction, using the CALDB 20260223 calibration. The final source and background event files were generated with circular regions with radii of 30″ around the source ($22^{h}\ 29^{m}\ 0\overset{s}{.}5260$, $61^{\circ}\ 14'\ 08\overset{''}{.}480$) and 80″ in a source-free region near the source, respectively. The total filtered exposure times for the archival (2020 September 23) and recent (2026 March 11) observations are approximately 45 ks and 25 ks, respectively.

2.3. NICER Observations

We used public archival data[18] from the NICER mission for our X-ray analysis, available on the HEASARC Browse interface. The available X-ray observing epochs range from MJDs 58872 to 60097 (ObsIDs 2579050915 to 6033370220), which partially overlap with our CHIME/Pulsar timing observations.

Those observations were processed using NICER's standard processing pipelines from HEASoft[19] and NICERSoft.[20] We first applied standard screening and calibration procedures to produce cleaned event files using `nicerl2`.[21] Then, we used `psrpipe.py` to filter the cleaned event files further with the following criteria: (a) overshoot count rate below 1.5 counts s^{-1} per detector, (b) undershoot count rate below 600 counts s^{-1} per detector, (c) space weather index below 5, and (d) magnetic cutoff rigidity of Earth's magnetic field above 1.5 GeV/c.

3. Timing Analysis

3.1. Glitch Detections

We identified all four glitch events in PSR J2229+6114 through our glitch monitoring campaign. To enable near-real-time detection of glitches for the campaign, we built a glitch alert system based on the capability of the CHAMPSS Timing Pipeline to perform algorithmic pulsar timing (see Section 4.3 of C. Andrade et al. 2025 for technical details). The pipeline automatically processes CHIME observations and extracts pulse TOAs. Then, it iteratively fits timing models to TOAs and adds parameters based on the F-test (C. Phillips & S. Ransom 2022). In this pipeline process, glitches are identified as sudden losses of phase coherence in timing solutions from one day to the next, triggering real-time alerts.

We identified the first three glitches in the CHIME/Pulsar dataset during the commissioning tests of our glitch alert system. The first two glitches both disrupted phase coherence in the timing solution and were therefore detected immediately during the testing. The third glitch event was identified by an unmodeled early arrival of TOAs (i.e., a sudden spin-up in frequency) during modeling of the relaxation behavior of the second glitch. The long-term timing solution reveals that the frequency change induced by the spin-up is enduring, thereby distinguishing the event from red-noise effects.

After the glitch alert system was commissioned, the fourth glitch occurred, manifesting as a sudden loss of phase coherence in the first postglitch TOA extracted from the CHAMPSS observation. Our alert system detected the phase discontinuity and issued an alert ∼30 minutes after the source's first transit following the glitch epoch at the CHIME telescope. The glitch event was confirmed by data recorded during subsequent transits after the glitch epoch.

3.2. Glitch Sizes

We measured glitch sizes by obtaining local timing solutions from TOAs within ±1 month of the four glitch epochs and fitting simple glitch models that include only the glitch epoch, the change in frequency ($\Delta\nu$), and the change in spin-down rate ($\Delta\dot{\nu}$), without any recovery components.

The postfit parameters are presented in Table 1. The preglitch spin-down parameters (ν and $\dot{\nu}$) were fitted using PINT (J. Luo et al. 2021) with an initial timing solution from the ATNF Pulsar Catalogue[22] (R. N. Manchester et al. 2005), using JPL DE405 Planetary Ephemerides and TT(TAI) time standard as implemented in PINT. Starting from preglitch models, the glitch parameters are derived using the Markov Chain Monte Carlo (MCMC) fitting routine embedded in PINT with `emcee` (D. Foreman-Mackey et al. 2013) to properly sample degeneracies in glitch parameters. The reported glitch parameters in Table 1 are therefore the medians, with uncertainties corresponding to the 16th–84th percentile interval, of the posterior distribution. The glitch epoch was included as a free parameter in the fit, with a uniform prior to constrain it to lie between the two consecutive TOAs before and after the glitch. The phase change at the glitch epoch is enforced to be zero.

There were ambiguities in our measurement of spin frequencies and glitch sizes. Because CHIME's transit nature yields TOAs sampled uniformly at one per sidereal day, ν values that differ by $\pm N/T_{\rm sid}$ are not distinguishable using phase-coherent timing, where N is an integer and $T_{\rm sid}$ is the sidereal day. The same ambiguity applies when measuring glitch amplitudes, as $\Delta\nu$ may be comparable to or larger than $1/T_{\rm sid}$. We applied the technique described by C. Andrade et al. (2025) to all reported pre- and postglitch timing solutions to ensure that the measured ν and $\Delta\nu$ values are not aliased. This technique first aligns multiple days of fold-mode observations using phase-coherent timing solutions. Then it stacks these observations in time–phase space to achieve a higher signal-to-noise ratio and measures the drift of pulse phases across individual transits induced by the aliased solutions.

Among the four glitch events reported in the table, the first glitch (at MJD 59267) was measured previously by E. Güger-cinoğlu et al. (2022), while the remaining three glitches are presented here for the first time. The size of the first glitch is similar to that reported previously, despite a small discrepancy that is primarily due to the two independent measurements fitted with a simple glitch model without exponential recovery to TOAs spanning different time intervals. The simple model effectively approximates the underlying exponential with a linear model and therefore measures $\Delta\nu$ and $\Delta\dot{\nu}$ slightly differently depending on which portion of the postglitch behavior is sampled.

Figure 1 shows residuals of TOAs surrounding all four glitch events compared to the preglitch models (i.e., the models without glitch parameters), overplotted with the fitted

[18] Observations were obtained from the General Observer (PI: W. Ho) and Director's Discretionary Time programs.
[19] Version 6.35.1; https://heasarc.gsfc.nasa.gov/docs/software/lheasoft/.
[20] Accessed on 2025 March 5; https://github.com/paulray/NICERsoft.
[21] Version 2025-03-11_V013a; https://heasarc.gsfc.nasa.gov/docs/nicer/analysis_threads/nicerl2/.
[22] Version 2.6.5; https://www.atnf.csiro.au/research/pulsar/psrcat/.

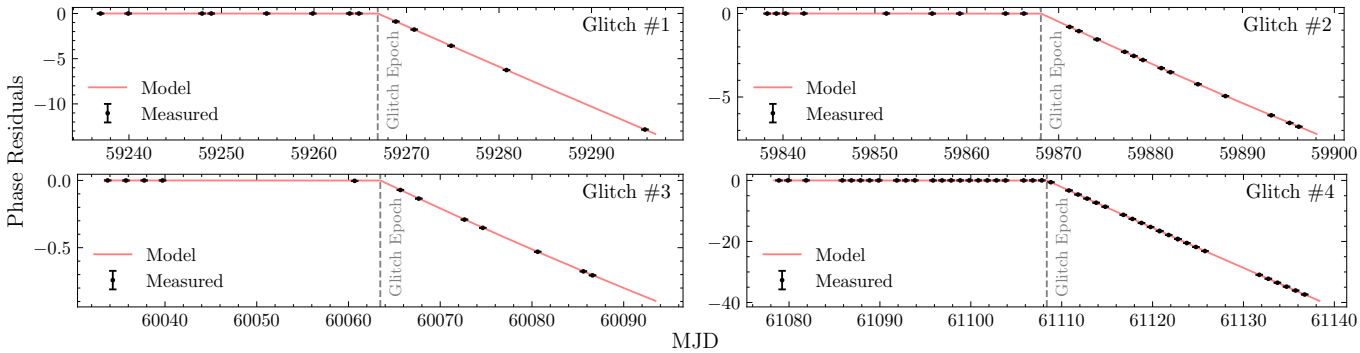

Figure 1. Timing residuals surrounding glitch epochs for PSR J2229+6114. Each panel corresponds to a glitch identified in our timing observations with the CHIME telescope, with glitch epochs indicated by dashed vertical lines. Simple glitch models that include only glitch epoch, $\Delta\nu$, and $\Delta\dot{\nu}$ are overplotted as a red solid line in the prefit residuals.

Table 1
Glitches Identified in CHIME/Pulsar Observations

#	Period Epoch (MJD)	ν (Hz)	$\dot{\nu}$ (10^{-11} Hz s^{-1})	Glitch Epoch (MJD)	$\Delta\nu$ (10^{-6} Hz)	$\Delta\dot{\nu}$ (10^{-13} Hz s^{-1})	$\Delta\nu/\nu$ (10^{-7})	$\Delta\dot{\nu}/\dot{\nu}$ (10^{-3})	$\Delta E_{\rm rot}$ (10^{42} erg)
1	59267.0	19.3526460(2)	−2.91964(7)	59266.890(2)	5.244(2)	−0.80(2)	2.710(1)	2.75(5)	4.007(2)
2	59867.0	19.35113496(5)	−2.91800(1)	59868.062(4)	2.969(2)	−1.44(1)	1.5341(9)	4.94(4)	2.268(1)
3	60060.0	19.35064994(9)	−2.92068(2)	60063.47(3)	0.375(2)	−0.23(2)	0.194(1)	0.78(7)	0.286(2)
4	61108.0	19.348009606(8)	−2.939003(3)	61108.360(1)	15.632(2)	−3.08(2)	8.080(1)	10.48(6)	11.940(2)

Note. Calculation of the change in rotational kinetic energy ($\Delta E_{\rm rot}$) uses a typically assumed moment of inertia of neutron stars $I = 10^{45}$ g cm^2 (D. R. Lorimer & M. Kramer 2004). The quoted uncertainties in $\Delta E_{\rm rot}$ reflect only the measurement uncertainties in ν and $\Delta\nu$, not the systematic uncertainty in the assumed moment of inertia.

simple glitch models. All four glitches exhibit a sudden increase in the spin frequency (spin-up). The sizes of glitches 1, 2, and 4 are an order of magnitude larger than that of the third event, resulting in a sudden loss of phase coherence in the timing solution at the time of detection (this phase wrap is not visible in the figure as we manually aligned the TOAs for visualization). The first three glitches exhibit notable long-term recovery in our archival CHIME/Pulsar data, which we discuss further in Section 3.3.

3.3. Glitch Recoveries

The CHIME/Pulsar dataset for glitches 1–3 spans from several months before the first glitch epoch to roughly a year after the third, and those three glitches exhibit evidence of long-term recovery in the dataset. We subsequently modeled each glitch's recovery using the full set of available CHIME/Pulsar TOAs with the longer timing baseline. Since the fourth glitch is newly discovered, it is not possible to perform a similar modeling due to its short postglitch timing baseline at the time of writing.

Table 2 shows postfit glitch models with exponential decay terms ($\tau_{\rm d}$ and $\nu_{\rm d}$) for glitch recoveries. Using the simple glitch models in Section 3.2 as a starting point, these postfit models are fitted jointly by phase-connecting all the TOAs from MJD 59204 to 60513. Model parameters are again derived with the MCMC method, and the reported values are posterior medians with 16th–84th percentile uncertainties. Glitches 1 and 2 exhibit more complex recoveries, so we fitted them with two sets of decay terms on different timescales. The relaxation of glitch 3 is simpler and can be well described by a single decay term. However, since the second glitch was interrupted by the third, parameter degeneracies leave the second glitch's longer recovery timescale poorly constrained. Hence, we fixed the timescale at 76.5 days (varying it by ±1 day did not significantly affect the remaining parameter estimates).

Table 2
Parameters of the Glitch Recovery Model

Parameter	Glitch #1	Glitch #2	Glitch #3
Glitch Epoch (MJD)	59266.867(1)	59867.941(6)	60063.49(3)
$\Delta\nu$ (Hz)	$1.321(1) \times 10^{-6}$	$1.343(3) \times 10^{-6}$	$1.43(9) \times 10^{-8}$
$\Delta\dot{\nu}$ (Hz s^{-1})	$2.112(2) \times 10^{-14}$	$3.1(2) \times 10^{-15}$	$1.04(2) \times 10^{-14}$
$\tau_{\rm d}^{(1)}$ (MJD)	136.46(8)	76.5 (fixed)	94.8(4)
$\nu_{\rm d}^{(1)}$ (Hz)	$4.965(1) \times 10^{-6}$	$1.858(5) \times 10^{-6}$	$3.334(8) \times 10^{-7}$
$\tau_{\rm d}^{(2)}$ (MJD)	29.20(8)	11.1(2)	⋯
$\nu_{\rm d}^{(2)}$ (Hz)	$-1.085(2) \times 10^{-6}$	$-2.89(4) \times 10^{-7}$	⋯

Note. The preglitch ν and $\dot{\nu}$ are the same as those for glitch 1 in Table 1.

To visualize those glitch models, we derived spin-frequency evolution from the phase offsets between adjacent TOAs (rather than measuring it directly from individual observations due to insufficient precision). The derived spin frequency evolution, along with the evolution predicted by glitch recovery models, is shown in the top panel of Figure 2. The first two glitches exhibit a short-term spin-up recovery soon after the glitch epoch, but later the recovery is dominated by the long-term spin-down recovery. The third glitch also shows a relaxation soon after the sudden spin-up during the relaxation of the second glitch. The bottom panel of the figure shows the postfit timing residuals of the glitch models. The fit has a reduced χ^2 of 44.3, with the excess being primarily due to variations in the residuals that are of low amplitude, likely due

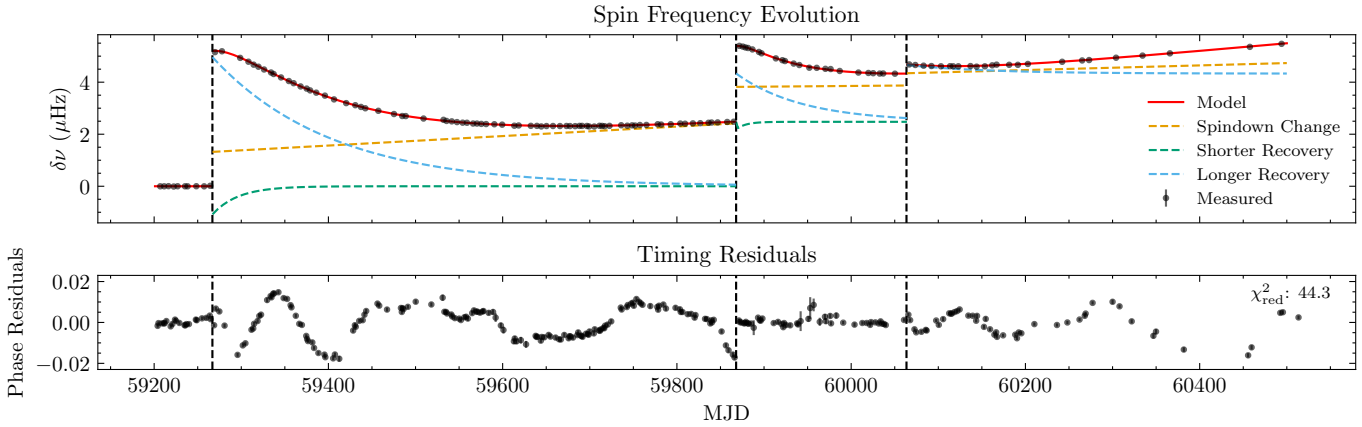

Figure 2. Spin frequency evolution of PSR J2229+6114 and its timing residuals in phase compared to glitch models with exponential recovery components. In the top panel, the frequency evolution is presented as the change in spin frequency relative to the prefit model prior to glitch 1. The measured spin frequencies are shown as black dots, and the postfit glitch model is shown as a red solid line underneath the black dots. Contributions from individual model components are indicated by colored dashed lines, as specified in the legend. Since the model for glitch 3 has only one long-term recovery component, no green dashed line (i.e., the shorter recovery) is plotted for the glitch. The postfit timing phase residuals are shown in the bottom panel. The postfit reduced χ^2 is indicated in the top right corner of the panel. Glitch epochs are shown by dashed black lines in both panels.

to inexact glitch modeling, and a smaller contribution from red noise. Nevertheless, those variations are centered at zero with an rms scatter of 0.006 in phase (0.6%), indicating a valid fit.

4. Radio Emission

4.1. Radio Profile Morphology

Figure 3 shows 5 day averaged pulse profiles before and after glitches 1–3 from 400 to 800 MHz, where preglitch, postglitch, and residuals are shown in each panel that corresponds to a detected glitch. To first obtain daily pulse profiles, we updated our fold-mode data using local timing solutions fitted by TOAs near glitch epochs, then averaged the frequency and time information using PSRCHIVE's `pam` routine. We subsequently used the `psradd` routine to sum the aligned daily profiles. We subtracted the baseline on each summed profile using the built-in function in PSRCHIVE. Since our profile amplitudes are not flux-calibrated, we rescaled each postglitch profile by the factor that minimizes the squared residual relative to the corresponding preglitch profile (i.e., by a factor of $\sum_i p_{0,i} p_{1,i} / \sum_i p_{1,i}^2$, where $p_{0,i}$ and $p_{1,i}$ are the preglitch and postglitch profile amplitudes at bin i). The residuals shown in the figure are calculated by subtracting the preglitch profile from the postglitch profiles. The reduced χ^2 values for the on-pulse region in residuals (with a null hypothesis that the residuals are consistent with white Gaussian noise) in all three glitches are $\sim$1, with a number of degrees of freedom of 100 (number of on-pulse bins minus 2), indicating no statistically significant variation in radio profiles before and after the glitches.

The long-term averaged pulse profiles in RPPs are usually highly stable. To identify potential transient morphological variations in short timescales, we compared individual profiles with preglitch morphology and plotted them in Figure 4. We have again updated the fold-mode data surrounding three glitch epochs using the local timing solutions and averaged them per day to obtain daily pulse profiles. For each glitch, to create a template for preglitch profile morphology, we summed individual preglitch profiles in Figure 4 with PSRCHIVE's `psradd`, then smoothed them with `pas`. Then, for each individual profile, we removed the

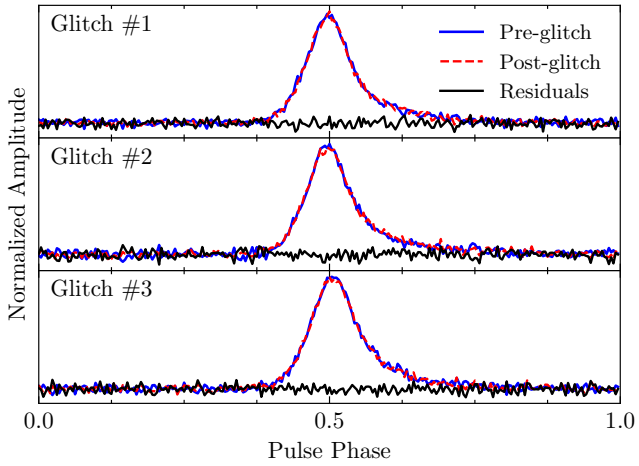

Figure 3. Radio pulse profiles of PSR J2229+6114 averaged over five days of CHIME/Pulsar observations before and after the respective glitch, where each panel corresponds to profiles around a different glitch. In each panel, the preglitch and postglitch average profiles are shown as blue solid and red dashed lines, respectively. The black solid line represents the residual between the two profiles, defined as the difference in amplitude between the post- and preglitch profiles.

baseline, scaled the template to match the profile's amplitude, as before, and computed the difference between the two profiles as the profile residuals. Finally, we again computed the reduced χ^2 values for the on-pulse region of each residual. The reduced χ^2 values in Figure 4 vary similarly before and after three glitches. There are two observations surrounding glitch 1 that show reduced χ^2 values that deviate from the noise by a statistically significant amount. However, since there is no clear structure in their corresponding residuals, we attribute the excessive χ^2 values to stochastic profile variations (e.g., pulse jitters).

A similar profile analysis is not possible for the fourth glitch because high-time-resolution timing observations of the source were not recorded prior to the glitch. Preglitch fold-mode observations for glitch 4 were recorded in 32 rotational phase bins by the CHAMPSS instrument, whereas CHIME/Pulsar observations with finer time resolution of 256 bins began only after the glitch was detected.

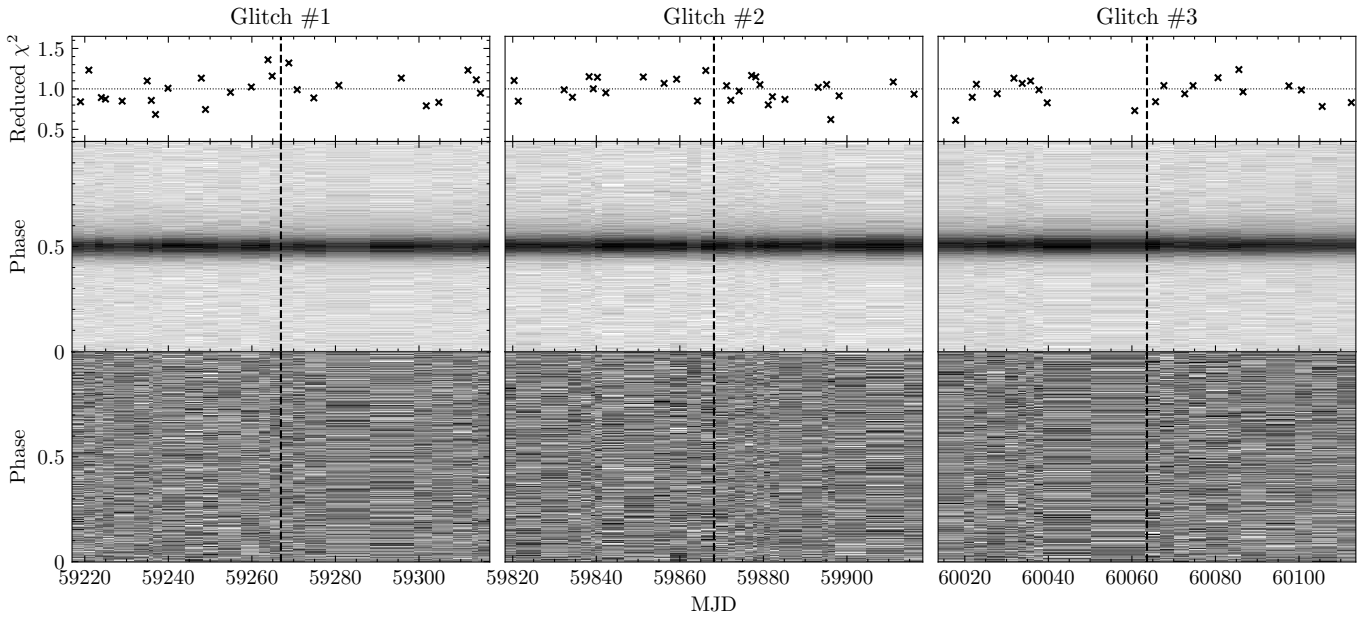

Figure 4. Radio pulse profile variations of PSR J2229+6114 in CHIME/Pulsar observations surrounding the epochs of glitches 1–3, with each subfigure for a different glitch. The middle and bottom panels in each subfigure show profiles and profile residuals (relative to the preglitch profile morphology) over time. The top panel presents the reduced χ^2 values of the on-pulse region in residuals as a function of time, with the horizontal dashed line denoting the reduced χ^2 at one. With 100 degrees of freedom, a reduced χ^2 of 1.25 deviates from the white-noise assumption at the $p < 0.05$ level, indicating statistically significant profile variation. The vertical dashed line indicates the epoch of each glitch.

4.2. Radio Bursts

In addition to analyzing the fold-mode data from CHIME/Pulsar, we also searched the CHIME/FRB database for bright single radio pulses from the source. CHIME/FRB is an all-sky, real-time survey for dispersed single pulses using the CHIME telescope, and focuses primarily on the discovery of fast radio bursts (FRBs) (see CHIME/FRB Collaboration et al. 2018 for technical details); it is also sensitive to giant radio pulses and single radio bursts from pulsars and magnetars (see CHIME/FRB Collaboration et al. 2020 and D. C. Good et al. 2021 for examples). By default, CHIME/FRB does not save raw data for known Galactic burst events, including pulsars, but it retains header information for every detected event in its database. The header information allows us to search for bursting behavior in PSR J2229+6114 by identifying an excess of events coincident with the source's sky position and DM values surrounding the glitch epoch.

We queried the CHIME/FRB database for single-pulse events registered between 2017 February 1 and 2026 April 1. Then we filtered these events using the following two criteria: (a) events labeled as PSR J2229+6114 by CHIME/FRB's Known Source Sifter (see Section 4.5 of CHIME/FRB Collaboration et al. 2018), and (b) events within a positional offset of $\pm 5°$ and a DM offset of $\pm 5\,\mathrm{pc\,cm^{-3}}$ from the pulsar. Our database query returned 172 candidate events, including some detected near the epoch of glitch 1. However, we determined that these events are spurious because their detection rates correlate with those at nearby sky positions, indicating poor localization, typical of RFI. Without any raw data being recorded, no further analysis can be done to verify the nature of these candidates. Thus, we conclude that our database query revealed no radio bursts clearly associated with the pulsar.

5. X-Ray Emission

5.1. X-Ray Fluxes

From the NICER dataset, we combined multiple observations into a single measurement to achieve a minimum exposure of 10 ks per data point, and measured the pulsed X-ray fluxes of the source over a 3 yr time span covering glitches 1–3. Those measurements are plotted as a function of time in Figure 5. The reduced χ^2 test indicates the pulsed flux is broadly consistent with the weighted mean of $0.041 \pm 0.002\,\mathrm{counts\,s^{-1}}$ ($\chi^2_{\mathrm{red}} = 1.24$, $p = 0.09$). The 3σ 0.5–10 keV upper limits for X-ray emission enhancement in glitches 1, 2, and 3 are 0.06 counts $\mathrm{s^{-1}}$, 0.08 counts $\mathrm{s^{-1}}$, and 0.07 counts $\mathrm{s^{-1}}$, respectively (corresponding to a fractional enhancement up to 2.4, 4.6, and 17.3 above the preglitch level, respectively, calculated from the nearest data point before and after the glitch in Figure 5). These upper limits show no statistically significant flux enhancement at the glitch epochs. If PSR J2229+6114 showed an enhancement in X-ray emission after glitches 1–3 at a similar level to the two previously detected radiative changes in a high-B pulsar, our dataset would have been sensitive enough to detect it (e.g., PSR J1846−0258 showed a fractional X-ray flux change $\Delta F_{\mathrm{X}}/F_{\mathrm{X}} \sim 7.7$). However, it should be noted the bin sizes in Figure 5 for the first data point after glitches 1, 2, and 3 are 15.2 days, 35.5 days, and 5.55 days, respectively; if a hypothetical flux enhancement had decayed on a very short timescale that is much shorter than bin sizes, we may not be able to capture the change in emission in this NICER dataset.

For the two NuSTAR observations, we extracted the spectra with `nuproducts` (see Section 2.2) and fitted them with an absorbed power-law model using XSPEC v12.15.1 (K. A. Arnaud 1996). The fitted spectral parameters are listed in Table 3 and the spectra are plotted in Figure 6. We used the 2020 September observation as our reference spectrum for the

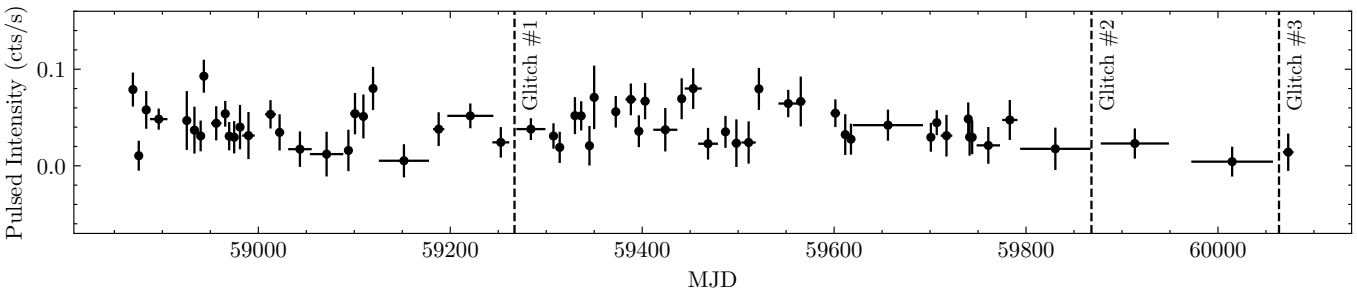

Figure 5. Pulsed 0.5–10-keV X-ray flux evolution of PSR J2229+6114 from archival NICER observations, covering glitches 1–3. Epochs of glitch events are indicated by vertical dashed lines. Multiple observations are combined into a single measurement to achieve at least 10 ks of exposure per data point. The time spans of the combined observations are indicated by the horizontal error bar.

era before glitch 4, as the observation (MJD 59113) was not known to be close in time to any known glitch in PSR J2229+6114 (A. Basu et al. 2022). The best-fit power-law indices (Γ_X) are consistent within 1σ, indicating no statistically significant spectral evolution between the two epochs. The postglitch 3–79 keV absorbed flux from the source is marginally lower than the preglitch level, with a difference of $\Delta F_X^{abs} = -1.0(3) \times 10^{-12}$ erg s^{-1} cm^{-2}. We therefore conclude that there is no evidence for an X-ray flux enhancement following glitch 4 in NuSTAR observations. To allow for comparison with previous measurements from other sources in Section 6, we place a 3σ upper limit on the unabsorbed flux enhancement in the 0.5–10 keV band of 0.03×10^{-12} erg s^{-1} cm^{-2} (corresponding to a fractional enhancement up to 0.03).

5.2. X-Ray Bursts

Some magnetars and high-B RPPs show short X-ray bursts (e.g., V. M. Kaspi et al. 2003; F. P. Gavriil et al. 2008) after glitch events. For this reason, we extracted the X-ray light curve with 5 ms time bins from the NICER (0.1–10 keV) and NuSTAR (3–79 keV) datasets and searched for short X-ray bursts exceeding the mean count rate by $>5\sigma$, assuming Poisson statistics. Our search identified seven burst-like candidate events in NICER observations, but they are likely not astrophysical. All seven candidates were detected by only one detector (of the 52 active detectors on board NICER), indicating they are likely due to instrumental artifacts or particle background. The NuSTAR search returned no candidates above threshold. We therefore find no significant detections of X-ray bursts that are clearly associated with the source.

5.3. X-Ray Profile Morphology

We folded NICER and NuSTAR observations to produce X-ray pulse profiles for PSR J2229+6114 before and after glitches 1 and 4, presented in Figures 7 and 8, respectively. A similar analysis is not possible for the remaining glitches 2 and 3 because they are too close in time; the surrounding NICER observations provide insufficient exposure to construct clear profiles.

In order to produce the 0.3–10 keV X-ray profiles presented in Figure 7, we averaged over ~1 yr of NICER observations before and after glitch 1. To phase-align NICER observations, we obtained a separate timing solution using radio TOAs from CHIME/Pulsar, covering the NICER observing epochs. This solution was derived by starting with our glitch models in Table 1 and fitting higher-order spin-frequency derivatives to suppress red noise in the timing residuals. While this approach introduces timing artifacts, these do not affect our X-ray analysis, which relies on phase alignment rather than timing precision. We subsequently calculated each photon's rotational phase with the ephemeris using `photonphase` in PINT (J. Luo et al. 2021) and binned the photons into pulse profiles.

We subtracted the two NICER pulse profiles and computed the reduced χ^2 of the resulting differences relative to zero (i.e., white Gaussian noise). In the 0.3–3.0 keV band, the residuals are consistent with Gaussian noise, indicating no statistically significant variation ($\chi^2_{red} = 1.12$, $p = 0.268$) for

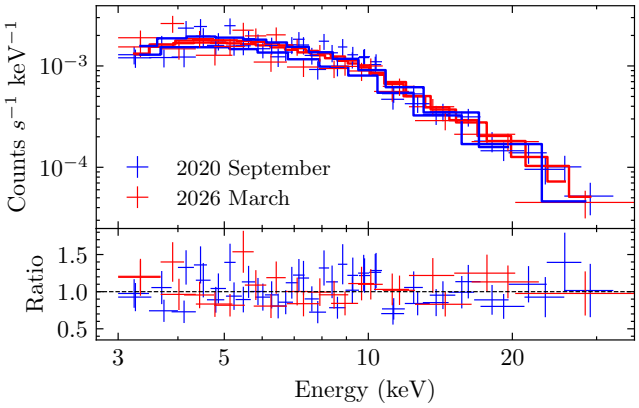

Figure 6. X-ray spectra of PSR J2229+6114 from two epochs of NuSTAR observations. The top panel presents the spectra from FPMA and FPMB before (blue) and after (red) glitch 4. The data for both epochs were fitted with a `tbabs*pow` model (see Table 3); the best-fit models are shown as solid lines. The bottom panel shows the ratio (unitless) of data to model (data/model), with a horizontal dashed line indicating a ratio of 1.

Table 3
NuSTAR Spectral Fitting Results

Parameter	2020 Sep	2026 Mar
Model	`tbabs*pow`	
N_H (10^{22} cm^{-2})[a]	0.89 (fixed)	
Γ_X	1.47 ± 0.06	1.61 ± 0.09
χ^2/dof	47/47	18/21
F_X^{abs} (10^{-12} erg s^{-1} cm^{-2})[b]	4.7 ± 0.2	$3.7^{+0.2}_{-0.3}$
F_X^{unabs} (10^{-12} erg s^{-1} cm^{-2})[c]	1.13 ± 0.03	1.01 ± 0.04

Notes. All quoted uncertainties correspond to 1σ confidence intervals.
[a] The hydrogen column density, taken from I. Pope et al. (2024) and fixed in the fit.
[b] The 3–79 keV absorbed X-ray fluxes, taken from an average of FPMA and FPMB.
[c] The 0.5–10 keV unabsorbed X-ray fluxes, calculated with the convolution `cflux` model.

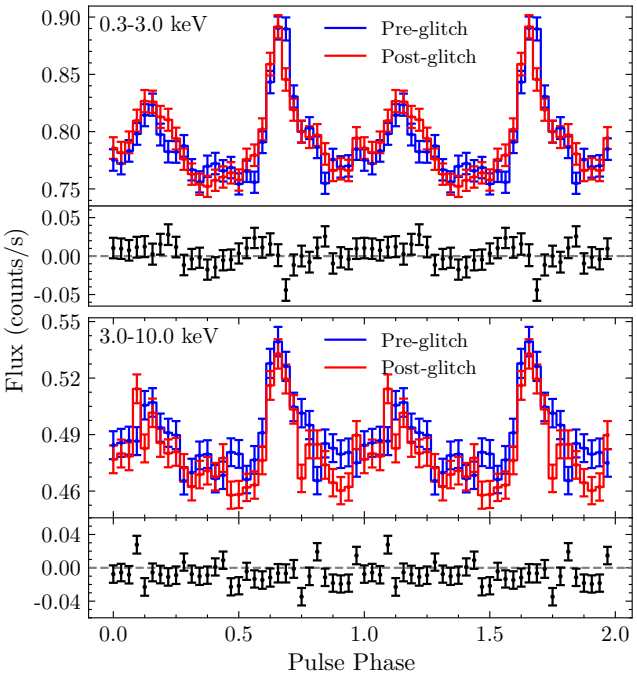

Figure 7. X-ray pulse profiles of PSR J2229+6114 accumulated over ∼1 yr of NICER observations before and after glitch 1. Profiles and their residuals in soft (0.3–3.0 keV) and hard (3.0–10.0 keV) X-rays are plotted in the top and bottom subfigures, respectively. In each subfigure, the top panel shows the preglitch (blue) and postglitch (red) profiles. The bottom panel shows the absolute residuals, obtained by subtracting the preglitch profile from the postglitch profile without normalization or median subtraction. Each profile is repeated for better visualization.

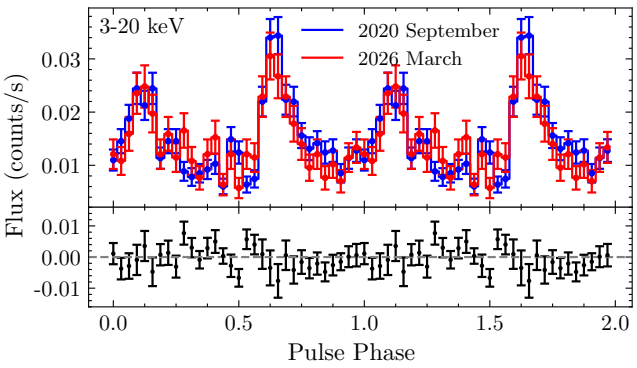

Figure 8. X-ray pulse profiles of PSR J2229+6114 from two epochs of NuSTAR observations. The top panel presents the profiles before (blue) and after (red) glitch 4 in hard X-rays (3–20 keV). The bottom panel shows the absolute profile residual. Each profile is repeated for better visualization.

glitch 1. Notably, despite the source exhibiting visually similar hard X-ray profiles before and after the glitch, residual analysis in the 3.0–10.0 keV band reveals a modest excess variation inconsistent with white noise ($\chi^2_{\rm red} = 1.94$, $p = 0.001$), suggesting possible evolution in the hard X-ray emission. However, it is possible that this excess variation is primarily due to the preglitch baseline flux being slightly brighter. If we normalize the two profiles in the hard X-ray band by subtracting the median fluxes from each phase bin, the residuals analysis again shows no statistically significant variation in their morphology ($\chi^2_{\rm red} = 1.42$, $p = 0.057$) across glitch 1. With this dataset, however, we cannot determine whether the baseline offset arises from the source or the background emission.

To produce the 3–20 keV X-ray profiles from NuSTAR, we again calculated the rotational phase of each photon using `photonphase`. For the preglitch epoch, we used a local timing solution fitted from CHIME/Pulsar radio TOAs surrounding the NuSTAR observation, starting from the preglitch timing solution of glitch 1 in Table 1. For the postglitch epoch, we used the local timing solution for glitch 4 in Table 1. In both models, we fitted the phase offset (relative to the radio pulse profile template from which TOAs are extracted) to align profiles from two epochs at the same rotational phase. We generated the pulse profile and residuals as before. The reduced χ^2 of the residuals suggests no statistically significant variation in profiles between the two epochs of NuSTAR observations ($\chi^2_{\rm red} = 0.99$, $p = 0.49$).

6. Discussion

Our analysis revealed no evidence of X-ray flux enhancement or short X-ray bursts following any of the four glitches in PSR J2229+6114. These results increase the number of rapid postglitch X-ray observations of RPPs from four to five. In this section, we present our results alongside previous similar measurements and discuss their implications in the context of the unifying neutron star model, in which the *B*-field is the unifying parameter.

Table 4 summarizes all rapid X-ray follow-ups of glitches in five RPPs to date. The two high-*B* RPPs exhibited magnetar-like outbursts immediately after glitch events, suggesting that these high-*B* RPPs are transitional objects between RPPs and magnetars: PSR J1846−0258 ($B_{\rm dip} \approx 5 \times 10^{13}$ G; E. V. Gotthelf et al. 2000) exhibited two large glitches in 2006 May and 2020 August, each accompanied by a magnetar-like outburst that lasted for ∼2 months (F. P. Gavriil et al. 2008; C.-P. Hu et al. 2023). PSR J1119−6127 ($B_{\rm dip} \approx 4 \times 10^{13}$ G; F. Camilo et al. 2000) showed a similar outburst in 2016 July immediately after a large glitch with $\Delta\nu/\nu = 5.74(8) \times 10^{-6}$ (R. F. Archibald et al. 2016). Both sources also exhibited a temporary transition to a magnetar-like X-ray spectrum during their outbursts (see discussion by R. F. Archibald et al. 2016 for a review). Indeed, the inferred *B*-field strength could serve as a unifying parameter for neutron stars, thereby bridging or perhaps unifying the perceived dichotomy between RPPs and magnetars in neutron star astrophysics (see V. M. Kaspi 2010 for a review).

Despite the detection of X-ray burst activity in two high-*B* RPPs at glitch epochs, confirmation of a unified picture requires consideration of behavior near the lower end of the high-*B* regime. It remains unclear whether this magnetar-like behavior is a general characteristic of most of the population and whether it scales with the inferred surface magnetic field strength. However, rapid postglitch X-ray follow-up of lower *B*-field RPPs ($B_{\rm dip} < 10^{13}$ G) has been rare due to observational challenges, including the need for high-cadence monitoring, despite more pulsars being discovered in the transitional regime than in the high-*B* regime. Prior to the NuSTAR follow-up of PSR J2229+6114 reported by this paper, such observations have thus far only occurred in the Vela pulsar ($B_{\rm dip} \approx 3 \times 10^{12}$ G; R. G. Dodson et al. 2002) and the Crab pulsar ($B_{\rm dip} \approx 4 \times 10^{12}$ G; B. Shaw et al. 2018; X. Zhang et al. 2018),[23] as listed in Table 4. All follow-up observations were triggered by glitch detections from

[23] Glitches in the Crab pulsar are special, exhibiting distinct properties such as delayed spin-ups, as well as correlated magnetospheric changes that suggest a possible magnetospheric contribution (see S. Zhou et al. 2022 for a review).

Table 4
Summary of X-Ray Follow-up of RPP Glitches

PSR	$B_{\rm dip}$[a] (G)	$\Delta\nu/\nu$	$\Delta E_{\rm rot}$[b] (erg)	$\Delta F_{\rm X}/F_{\rm X}$[c]	References
B0531+21	3.8×10^{12}	4.8×10^{-7}	1.7×10^{43}	...	(1, 2, 3)
B0833−45	3.4×10^{12}	3.1×10^{-6}	1.5×10^{43}	...	(4)
J1119−6127	4.1×10^{13}	5.8×10^{-6}	1.4×10^{42}	160	(5, 6)
J1846−0258	4.9×10^{13}	6.2×10^{-6}	2.3×10^{42}	7.7	(7, 8, 9)
J2229+6114	2.0×10^{12}	8.1×10^{-7}	1.2×10^{43}	<0.03	(10, this work)

Notes. Parameters corresponding to the largest glitch from each source for which X-ray follow-up observations have been made.
[a] The inferred surface B-field, taken from the ATNF pulsar catalog (R. N. Manchester et al. 2005).
[b] The change in rotational kinetic energy due to the glitch, computed as $\Delta E_{\rm rot} \approx 4\pi^2 I \nu \Delta\nu$, assuming a canonical moment of inertia $I = 10^{45}$ g cm^2 for all sources and that the neutron star rotates uniformly as a rigid body.
[c] The fractional enhancement in 0.5–10 keV unabsorbed X-ray fluxes, with 3σ upper limits for nondetections and "..." where no constraint was placed.
References. (1) A. G. Lyne et al. (2015); (2) B. Shaw et al. (2018); (3) X. Zhang et al. (2018); (4) R. G. Dodson et al. (2002); (5) R. F. Archibald et al. (2016); (6) P. Weltevrede et al. (2011); (7) M. A. Livingstone et al. (2011); (8) M. A. Livingstone et al. (2007); (9) F. P. Gavriil et al. (2008); (10) D. A. Smith et al. (2023).

dedicated monitoring campaigns. A measurable glitch-induced change in X-ray emission was found in neither RPP, supporting the idea that glitch-related magnetar-like emission is likely unique to, or at least most common in, high-B RPPs.

It is worth noting that all three glitches from lower B-field RPPs in Table 4 have smaller fractional frequency changes ($\Delta\nu/\nu$) than the two glitches in high-B RPPs, but their changes in rotational kinetic energy ($\Delta E_{\rm rot}$) are all greater than those seen in the two high-B RPPs. This suggests that the bursting behavior in high-B RPPs may be independent of the glitch's change in rotational kinetic energy, despite their strong connection with glitch events. The lack of dependence on changes in rotational kinetic energy is consistent with the model prediction of R. Perna & J. A. Pons (2011) that the bursting behavior in neutron stars is instead driven by the elastic energy accumulated in their crust, which is probably released via starquakes. However, the mechanism linking bursting behavior to glitches remains an open question.

The data currently support more dramatic postglitch emission activity in high-B RPPs, as in magnetars, but the statistics are still limited to constrain the underlying relationship between B-field and outburst. The X-ray follow-ups listed in Table 4 thus far are both for sources with conventional spin-inferred B-fields and for those with much higher values; how the postglitch emission behavior in RPPs changes with B-fields in the intermediate—likely transitional—regime (from 4×10^{12} to 4×10^{13} G) remains unclear. It is also unknown whether there are any hidden parameters, in addition to the B-field strength, that relate to the postglitch emission activity in RPPs (e.g., multipolar fields, characteristic ages). Thus, future nondetections or weak detections of postglitch emission in RPPs are essential for mapping any continuous relationship that could break the dichotomous classification of RPPs and magnetars in neutron star astrophysics.

7. Conclusions and Future Prospects

We have presented the first result from our pulsar glitch monitoring campaign with the CHIME telescope, which analyzed the radio and X-ray emission surrounding four glitch events in PSR J2229+6114. Among the four events, the first three were identified in archival CHIME/Pulsar data, and the fourth was detected by our glitch alert system immediately after its first transit since the glitch epoch. Our analysis showed no evidence of X-ray flux enhancement following any of the four glitches in PSR J2229+6114. We also found no changes in profile morphology (glitches 1 and 4 in X-rays and glitches 1–3 in the radio band) and no bursts in either band. These postglitch radiative behaviors are in stark contrast to the significant changes in X-ray and radio emission observed after comparable glitches in RPPs with much higher magnetic fields.

Using radio datasets, we measured the glitch epochs and sizes for all four glitch events and modeled the long-term relaxation behavior for the first three glitches with longer timing baselines. We also compared the morphology of the radio profiles before and after the first three glitch events using high-resolution CHIME/Pulsar observations and found no significant profile variations. To search for evidence of glitch-induced radio bursts, we queried the CHIME/FRB database and found that none of the candidate events detected by the system were clearly associated with the source. From X-ray datasets, we measured the flux evolution for all four glitch events, found no evidence for X-ray flux enhancement, and reported 3σ upper limits on any such enhancement. We also searched for short X-ray bursts in X-ray light curves and found none that were clearly associated with the source's emission. Additionally, we compared the source's X-ray pulse profile before and after glitches 1 and 4, finding no significant variations in profile morphology, except for a slight baseline offset in glitch 1's hard X-ray profile, the origin of which could not be determined.

The absence of radiative change after glitches in PSR J2229+6114, an RPP with a lower B-field than PSRs J1846−0258 and J1119−6127, is consistent with predictions of a unifying neutron star model in which the B-field strength serves as the unifying parameter. This supports the idea that postglitch radiative changes in RPPs are probably unique to or at least most common among those with a high B-field. However, our discussion demonstrated that X-ray follow-up of RPPs after glitches remains worthwhile, particularly in the mid- to high-B regime. Our pulsar glitch monitoring campaign is currently observing 20 high-B RPPs with $B_{\rm dip} > 5 \times 10^{12}$ G at daily cadence, and this number will grow as ongoing all-sky pulsar surveys in the Northern Hemisphere (e.g., the CHAMPSS Survey; C. Andrade et al. 2025) discover more new pulsars in the high-B regime. In the future, we expect the campaign to capture large glitch events within 48 hr of their occurrence and to trigger rapid X-ray follow-up through ToO observations. It may also enable near-simultaneous radio and X-ray follow-up

during glitch epochs. We hope this effort will improve our statistics and thereby impose further constraints on postglitch behavior of those RPPs in the likely transitional B-field regime from 4×10^{12} to 4×10^{13} G.

Acknowledgments

M.N. is a Fonds de Recherche du Quebec—Nature et Technologies (FRQNT) postdoctoral fellow. V.M.K. holds the Lorne Trottier Chair in Astrophysics & Cosmology, a Distinguished James McGill Professorship, and receives support from an NSERC Discovery grant (RGPIN 228738-13). The AstroFlash research group at McGill University, University of Amsterdam, ASTRON, and JIVE is supported by: a Canada Excellence Research Chair in Transient Astrophysics (CERC-2022-00009); an Advanced Grant from the European Research Council (ERC) under the European Union's Horizon 2020 research and innovation program ("EuroFlash;" grant agreement No. 101098079); an NWO-Vici grant ("AstroFlash;" VI.C.192.045); an ERC Starting Grant ("EnviroFlash;" grant agreement No. 101223057); and an NWO-Veni grant (VI.Veni.222.295). A.C. holds a UBC 4-Year Fellowship. E.F. is supported by the National Science Foundation (NSF) under grant No. AST-2407399. D.C.G. is supported by NSF Astronomy and Astrophysics Grant (AAG) award #2406919. A.B.P. acknowledges support by NASA through the NASA Hubble Fellowship grant HST-HF2-51584.001-A awarded by the Space Telescope Science Institute, which is operated by the Association of Universities for Research in Astronomy, Inc., under NASA contract NAS5-26555. A.B.P. also acknowledges prior support from a Banting Fellowship, a McGill Space Institute (MSI) Fellowship, and a Fonds de Recherche du Quebec—Nature et Technologies
(FRQNT) Postdoctoral Fellowship. Pulsar research at UBC is supported by an NSERC Discovery Grant and by the Canadian Institute for Advanced Research.

ORCID iDs

Wenke Xia https://orcid.org/0009-0009-9343-4193
Robert Main https://orcid.org/0000-0002-7164-9507
Mason Ng https://orcid.org/0000-0002-0940-6563
Victoria M. Kaspi https://orcid.org/0000-0001-9345-0307
Jason W. T. Hessels https://orcid.org/0000-0003-2317-1446
Alyssa Cassity https://orcid.org/0009-0007-0757-9800
Abigail K. Denney https://orcid.org/0009-0004-5775-8821
Emmanuel Fonseca https://orcid.org/0000-0001-8384-5049
Deborah C. Good https://orcid.org/0000-0003-1884-348X
Ajay Kumar https://orcid.org/0009-0002-0330-9188
Lars Künkel https://orcid.org/0000-0003-4634-5453
Bradley W. Meyers https://orcid.org/0000-0001-8845-1225
Aaron B. Pearlman https://orcid.org/0000-0002-8912-0732
Ingrid Stairs https://orcid.org/0000-0001-9784-8670

References

Andrade, C., Boyle, P. J., Brar, C., et al. 2025, ApJ, 990, 50
Archibald, R. F., Kaspi, V. M., Tendulkar, S. P., & Scholz, P. 2016, ApJL, 829, L21
Arnaud, K. A. 1996, ASPC, 101, 17
Basu, A., Shaw, B., Antonopoulou, D., et al. 2022, MNRAS, 510, 4049
Brook, P. R., Karastergiou, A., McLaughlin, M. A., et al. 2018, ApJ, 868, 122
Camilo, F., Kaspi, V. M., Lyne, A. G., et al. 2000, ApJ, 541, 367
CHIME Collaboration, Amiri, M., Bandura, K., et al. 2022, ApJS, 261, 29
CHIME/FRB Collaboration, Amiri, M., Bandura, K., et al. 2018, ApJ, 863, 48
CHIME/FRB Collaboration, Andersen, B. C., Bandura, K. M., et al. 2020, Natur, 587, 54
CHIME/Pulsar Collaboration, Amiri, M., Bandura, K. M., et al. 2021, ApJS, 255, 5
Dodson, R. G., McCulloch, P. M., & Lewis, D. R. 2002, ApJL, 564, L85
Foreman-Mackey, D., Hogg, D. W., Lang, D., & Goodman, J. 2013, PASP, 125, 306
Gavriil, F. P., Gonzalez, M. E., Gotthelf, E. V., et al. 2008, Sci, 319, 1802
Good, D. C., Andersen, B. C., Chawla, P., et al. 2021, ApJ, 922, 43
Gotthelf, E. V., Vasisht, G., Boylan-Kolchin, M., & Torii, K. 2000, ApJL, 542, L37
Gügercinoğlu, E., Ge, M. Y., Yuan, J. P., & Zhou, S. Q. 2022, MNRAS, 511, 425
Halpern, J. P., Camilo, F., Gotthelf, E. V., et al. 2001, ApJL, 552, L125
Hotan, A. W., van Straten, W., & Manchester, R. N. 2004, PASA, 21, 302
Hu, C.-P., Kuiper, L., Harding, A. K., et al. 2023, ApJ, 952, 120
Jennings, R. J., Cordes, J. M., Chatterjee, S., et al. 2024, ApJ, 964, 179
Kaspi, V. M. 2010, PNAS, 107, 7147
Kaspi, V. M., & Beloborodov, A. M. 2017, ARA&A, 55, 261
Kaspi, V. M., Gavriil, F. P., Woods, P. M., et al. 2003, ApJL, 588, L93
Livingstone, M. A., Kaspi, V. M., Gavriil, F. P., et al. 2007, Ap&SS, 308, 317
Livingstone, M. A., Ng, C., Kaspi, V. M., Gavriil, F. P., & Gotthelf, E. V. 2011, ApJ, 730, 66
Lorimer, D. R., & Kramer, M. 2004, Handbook of Pulsar Astronomy, Vol. 4 (Cambridge Univ. Press)
Luo, J., Ransom, S., Demorest, P., et al. 2021, ApJ, 911, 45
Lyne, A. G., Jordan, C. A., Graham-Smith, F., et al. 2015, MNRAS, 446, 857
Manchester, R. N., Hobbs, G. B., Teoh, A., & Hobbs, M. 2005, AJ, 129, 1993
Morello, V., Barr, E. D., Cooper, S., et al. 2019, MNRAS, 483, 3673
Perna, R., & Pons, J. A. 2011, ApJL, 727, L51
Phillips, C., & Ransom, S. 2022, AJ, 163, 84
Pope, I., Mori, K., Abdelmaguid, M., et al. 2024, ApJ, 960, 75
Shaw, B., Lyne, A. G., Stappers, B. W., et al. 2018, MNRAS, 478, 3832
Smith, D. A., Abdollahi, S., Ajello, M., et al. 2023, ApJ, 958, 191
Weltevrede, P., Johnston, S., & Espinoza, C. M. 2011, MNRAS, 411, 1917
Zhang, X., Shuai, P., Huang, L., Chen, S., & Du, Y. 2018, ApJ, 866, 82
Zhou, S., Gügercinoğlu, E., Yuan, J., Ge, M., & Yu, C. 2022, Univ, 8, 641